RANS Turbulent Model Assessment for Fan Array Wind Tunnel Facilities

Bryan Mendoza,* Brandon Burnett,† Jayce Fiene,‡ Fernado Rivera§ and Daniel Foti¶
Department of Mechanical Engineering, University of Memphis, Memphis, Tennessee 38152

The testing of unmanned aerial vehicles in unpredictable environments poses significant repeatability issues due to a lack of environmental control. Fan array wind tunnels provide a controlled, laboratory-scale flow field with a large testing section. However, the development of the flow is subject to the dimensions of the facility laboratory where the wind tunnel is located. In this study, we employ Reynolds-Averaged Navier-Stokes (RANS) simulations to analyze and assess the aerodynamic performance and facility influence on the flow produced by a fan array wind tunnel. A recent study [Rahmati, et al., AIAA 2026-2307 AIAA SCITECH Forum, 2026] showed that while RANS predicts many of the large features, it is unable to capture the multi-scaled nature of the fan array jet as observed from experiments. We assess grid resolution and test a range of RANS turbulence models to attempt to better predict the effects of shear layers and jet interaction. We evaluate how the flow field, specifically the jet far field where testing would take place, is influenced by different fan array wind tunnel locations, fan operating speeds, and the facility dimensions. Our goal is to improve the ability of our computing model so that it will accurately predict and agree with the physical test results of various laboratory-scale wind wall tests.

I. Introduction

Unmanned aerial vehicles (UAVs) and unmanned systems (UxS) are increasingly deployed in complex environments where aerodynamic stability and robust flight control are critical for safe operation. However, real-world flight testing is costly, difficult to repeat, and poses significant risks during early-stage design and development. These reasons motivate the impetus to acquire and characterize laboratory testing environments where repeatability and control are possible. While conventional wind tunnels provide repeatable aerodynamic testing [1–6], there are limitations due to the presence of an enclosed test section, which provides insufficient space for full-scale UxS testing and near full-scale maneuvers. Reproducing realistic atmospheric turbulence and shear profiles requires calibrated equipment, such as active flow control and grids. However, the enclosure wind tunnel test section is the major constraint.

Recently, new developments in fan-array wind tunnel facilities [7–9] offer an alternative by generating spatially and temporally varying flow fields over large open test sections. They offer the repeatability of traditional wind tunnels with the open test section of field testing. Machine learning and testing enable the ability to model atmospheric data [10, 11] and other pertinent test conditions [7, 12, 13].

However, the flow development in fan-array facilities is strongly influenced by the surrounding laboratory geometry, including wall proximity and ceiling height, which can affect turbulence structure and jet interaction [14]. Accurate characterization of these facility-induced effects is essential for interpreting the experimental results and for future facility design. Furthermore, the Ref. [14], which employed Reynolds-Averaged Navier-Stokes (RANS) simulation with actuator disk parameterization to model the fan array and facility, showed that key differences in measurements and the simulations exist due to the multi-scale turbulence produced by the fan jet shear layers. These include (1) that the outer shear of the fan array does not dissipate as quickly as RANS predicts, (2) the size of the array strongly influences the jet development, and (3) RANS prediction using the $k-\omega$ turbulence model resembles canonical jet development or small jet arrays regardless of the size of the simulated array. Overall, the simulations are too dissipative and do not capture the fan array jet regimes accurately.

In this work, we will assess different RANS turbulence models for the University of Memphis fan array wind tunnel facility. The previously employed $k-\omega$ model [15] in the Ref. [14] will be compared with $k-\epsilon$ models. The former is

*Undergraduate Student, Department of Mechanical Engineering, AIAA Student Member Number 1400317
†Undergraduate Student, Department of Mechanical Engineering, AIAA Student Member Number 1823363
‡Undergraduate Student, Department of Mechanical Engineering, AIAA Student Member Number 1930934
§Undergraduate Student, Department of Mechanical Engineering, AIAA Student Member Number 1930869
¶Associate Professor, Department of Mechanical Engineering, AIAA Member

better-suited for wall-bounded flows, while the latter has been used extensively in high-Re free shear layer flows. As fan array wind tunnel facilities have both walls and free shear layers, there are outstanding questions about the efficacy of either model. This paper is set up with numerical methods and RANS turbulence models described in section II, the description of the University of Memphis facility and its discretization in section III, the results are presented in section IV, and conclusions are discussed in section V.

II. Numerical Methods

The *pimpleFoam* solver within OpenFOAM [16], is employed to investigate the flow from a fan array wind tunnel facility. It solves the pressure-velocity coupling equation using the PIMPLE algorithm [17]. The PIMPLE algorithm is a hybrid approach of both the PISO (Pressure-Implicit with Splitting of Operators) [18, 19] and SIMPLE (Semi-Implicit Method for Pressure-Linked Equations) [20] algorithms. The PIMPLE algorithm obtains a fully converged steady-state solution before marching in time. In the SIMPLE algorithm, the steady-state Navier-Stokes equations are solved using a repetitive method. Initially, a pressure field is guessed, and the momentum equation is solved using the guessed pressure to obtain an intermediate velocity field. Using the Poisson equation [21], by forcing the continuity, the pressure is corrected, and then the velocity field is adjusted. Both pressure and velocity fields are updated in a loop until convergence. Unlike the SIMPLE algorithm, the PISO algorithm is suitable for transient problems. It includes multiple pressure-velocity correction steps (inner corrections) in each time step. In a PIMPLE loop, the time step is adjusted based on the CFL number. If multiple inner corrections with only one outer correction are used, the PIMPLE loop resembles the PISO. On the other hand, if multiple outer corrections with only one inner correction is used, it makes the loops similar to the SIMPLE algorithm.

The RANS continuity and momentum equations for the incompressible flow solved in the pimpleFoam algorithm are the following ($i, j = 1, 2, 3$, repeated indicies implies summation):

$$\frac{\partial \bar{u_i}}{\partial x_i} = 0 \tag{1}$$

$$\frac{\partial \bar{u_i}}{\partial t} + \frac{\partial \bar{u_i}\bar{u_j}}{\partial x_j} = -\frac{1}{\rho}\frac{\partial \bar{p}}{\partial x_j} + \frac{\partial}{\partial x_j}\left[\nu\left(\frac{\partial \bar{u_i}}{\partial x_j} + \frac{\partial \bar{u_j}}{\partial x_i}\right)\right] - \frac{\partial \tau_{ij}}{\partial x_j}, \tag{2}$$

where u_i is the mean velocity vector, p is the pressure, and ν is the kinematic viscosity. The final term, $\frac{\partial \tau_{ij}}{\partial x_j}$, is the Reynolds stress term, which requires closure for through turbulence models.

A. RANS Turbulence Models

To model the turbulence, we employ four different turbulence models. All models are two-equation RANS models that compute the eddy viscosity ν_t to close the Reynolds stresses as follows:

$$\tau_{ij} = 2\nu_t S_{ij} - \frac{2}{3}k\delta_{ij}, \tag{3}$$

where k is the turbulent kinetic energy. Based on the work in Ref. [14], the $k-\omega$-SST model is employed, and ω is the specific dissipation rate. The other three equations are based on the $k-\epsilon$ model, where ϵ is the dissipation rate. Note that a relationship between the two dissipation terms is $\epsilon \sim \omega k$. This leads to two different equations to obtain the eddy viscosity:

$$\nu_t = C_\mu \frac{k^2}{\epsilon} \quad \text{or} \quad \nu_t = C_\mu \frac{k}{\omega}, \tag{4}$$

where C_μ is a coefficient specific to each model.

1. $k-\omega$ SST model

The $k-\omega$ SST model, which is a hybrid model, is classified under the Reynolds-averaged Navier–Stokes (RANS) category. The model switches to $k-\omega$ in the near-wall region, where the viscous forces are dominant, and to $k-\epsilon$ in the shear-free flow, where viscous forces are negligible. Based on the Menter ([15, 22]) with updated coefficients, the transport equations are computed using the following:

$$\frac{\partial(\rho k)}{\partial t} + \frac{\partial(\rho u_i k)}{\partial x_i} = \tilde{P}_k - \beta^* \rho k\omega + \frac{\partial}{\partial x_i}\left[(\mu + \sigma_k \mu_t)\frac{\partial k}{\partial x_i}\right] \tag{5}$$

$$\frac{\partial(\rho\omega)}{\partial t} + \frac{\partial(\rho u_i \omega)}{\partial x_i} = \alpha\rho S^2 - \beta\rho\omega^2 + \frac{\partial}{\partial x_i}\left[(\mu + \sigma_\omega \mu_t)\frac{\partial \omega}{\partial x_i}\right] + 2\left(1 - F_1\right)\rho\sigma_{w2}\frac{1}{\omega}\frac{\partial k}{\partial x_i}\frac{\partial \omega}{\partial x_i}, \tag{6}$$

where F_1 is the first blending function. Coefficients are set as $\beta^* = 0.09$, $\sigma_k = 0.85$, $\sigma_\omega = 0.5$, $\sigma_{\omega,2} = 0.856$, and $\alpha = 5/9$.

2. $k - \epsilon$

The $k - \epsilon$ model is designed for high-Re number flows away from walls. Unlike the $k - \omega$, wall shear stresses are not predicted well without the use of wall functions. The model is based on Ref. [23]. The transport equations are the following: 1. Turbulent Kinetic Energy

$$\frac{\partial k}{\partial t} + u_i \frac{\partial k}{\partial x_i} - \frac{\partial}{\partial x_i}\left[\left(\nu + \frac{\nu_t}{\sigma_k}\right)\frac{\partial k}{\partial x_i}\right] = P_k - \epsilon, \tag{7}$$

$$\frac{\partial \epsilon}{\partial t} + u_i \frac{\partial \epsilon}{\partial x_i} - \frac{\partial}{\partial x_i}\left[\left(\nu + \frac{\nu_t}{\sigma_\epsilon}\right)\frac{\partial \epsilon}{\partial x_i}\right] = C_{\epsilon 1}\frac{\epsilon}{k}P_k - C_{\epsilon 2}\frac{\epsilon^2}{k}, \tag{8}$$

where coefficients eddy viscosity $C_\mu = 0.09$, production of dissipation $C_{\epsilon 1} = 1.44$, destruction of dissipation $C_{\epsilon 2} = 1.92$, turbulent Prandtl number for k $\sigma_k = 1.0$, and turbulent Prandtl number for ϵ $\sigma_\epsilon = 1.3$.

3. Realizable $k - \epsilon$

In the previous model, $C_\mu = 0.09$ is a constant. In Realizable $k - \epsilon$ [24], C_μ is assumed to be a variable and depends on the mean strain and rotation rates. The equation is given as follows

$$C_\mu = \frac{1}{A_0 + A_s \frac{kU^*}{\epsilon}}, \tag{9}$$

where U^* adn A_s are functions of the mean strain rate (S_{ij}) and the mean rotation tensor (Ω_{ij}). The constraint helps prevent unphysical results in regions where the flow is stretching or rotating rapidly. The coefficient $A_0 = 4.0$. The other coefficients in the standard model are production of dissipation $C_{\epsilon 1} = 1.44$, destruction of dissipation $C_{\epsilon 2} = 1.9$ are changed to turbulent Prandtl number for k $\sigma_k = 1.0$, and turbulent Prandtl number for ϵ $\sigma_\epsilon = 1.2$.

4. RNG $k - \epsilon$

The RNG (Renormalization Group) $k - \epsilon$ [25] is also closely related to the standard model above. While the standard $k - \epsilon$ constants are derived from empirical data, the RNG constants are derived from renormalization group theory [26]. The additional assumption is that the ϵ equation gains an additional term, R_ϵ, which makes the model more responsive to rapid changes in strain.

$$\frac{\partial \epsilon}{\partial t} + u_i \frac{\partial \epsilon}{\partial x_i} - \frac{\partial}{\partial x_i}\left[\left(\nu + \frac{\nu_t}{\sigma_\epsilon}\right)\frac{\partial \epsilon}{\partial x_i}\right] = C_{\epsilon 1}\frac{\epsilon}{k}P_k - C_{\epsilon 2}\frac{\epsilon^2}{k} - R_\epsilon, \tag{10}$$

where R_ϵ is calculated as

$$R_\epsilon = \frac{C_\mu \eta^3 (1 - \eta/\eta_0)}{1 + \beta\eta^3}\frac{\epsilon^2}{k}, \tag{11}$$

where η is a function of k and ϵ, $\eta_0 = 4.38$, and $\beta = 0.012$. Coefficients of the model are changed to eddy viscosity $C_\mu = 0.0845$, production of dissipation $C_{\epsilon 1} = 1.42$, destruction of dissipation $C_{\epsilon 2} = 1.68$, turbulent Prandtl number for k $\sigma_k = 0.719$, and turbulent Prandtl number for ϵ $\sigma_\epsilon = 0.719$.

III. Case Setup

The layout of the University of Memphis fan array facility in the UAV and Remote Sensing Laboratory is simplified to include only the main laboratory walls, floor, ceiling, and the fan array. This simplified configuration, as shown in Fig. 1, was used for the computational model in previous work [14] and remains fixed across all turbulence model cases. The domain is closed with no inlets or outlets. With the described layout, recirculation patterns and return flow paths develop into a relatively steady-state configuration. This approach allows the jet dynamics induced by the fan array and modeled with RANS to be the focus of this, rather than being artificially constrained by cross-flow or inflow conditions.

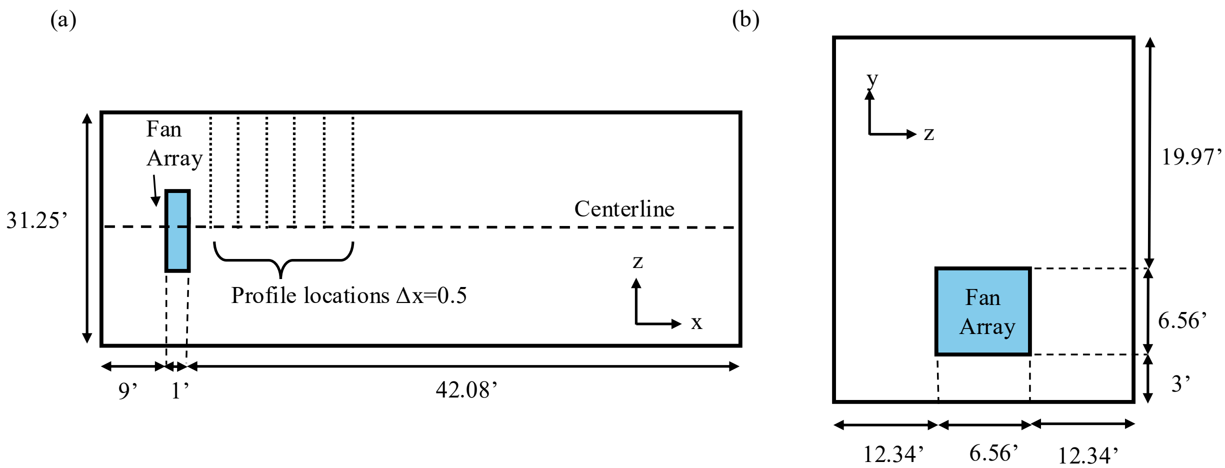

Fig. 1 (a) Top view and (b) side view of the layout and computational domain with dimensions of the University of Memphis facility. Dashed lines are shown to define the centerline and profile locations used below.

We simulate a 25×25 array of fans. The array is currently set on a table that allows air flow on all sides, so there is no pedestal modeled for this case. The dimensions of the array are $6.56' \times 6.56'$ and centered in the y-z plane. The FAWT is located $3'$ off the ground to reduce the effects from the ground on either the suction or pressure side.

A. Computational Grid and Boundary Conditions

The computational domain is discretized using a predominantly hexahedral mesh generated with OpenFOAM’s blockMesh utility. A graded meshing strategy is applied to improve resolution in regions with higher expected velocity gradients, particularly near the fan array plane and within inter-jet shear interaction zones. The mesh resolution is identical for all turbulence model cases to ensure that observed differences arise solely from turbulence model formulation.

All solid surfaces within the computational domain, including the laboratory walls, floor, and ceiling, are modeled as no-slip boundary conditions.

B. Fan Array Parameterization

To model the fan array, the actuator disk parameterization is employed. Rather than explicitly resolving blade geometry, each of the 25×25 fans was represented as an individual thin disk region in which a distributed body force is applied to the momentum equation. A constant thrust coefficient, $C_T = 0.16$, which corresponds to 45% duty cycle on the fan, is used, similar to Ref. [14]. This approach captures the overall thrust generation of the fan array without incurring the significant computational cost associated with resolving rotating blades and detailed near-wake structures. All simulations were conducted under steady, uniform fan output conditions in order to isolate mean-flow behavior and more clearly assess turbulence model performance.

IV. Results

To evaluate the sensitivity of the turbulence model in predicting jet interaction and centerline velocity decay, three new $k-\epsilon$-based turbulence models are investigated for the 25×25 fan array configuration: the standard model $k-\epsilon$ model, the RNG $k-\epsilon$ model, and the realistic model $k-\epsilon$ model. In previous simulations [14] ($k-\omega$ SST), a steep drop-off in centerline velocity was observed when compared to experimental measurements obtained from physical fan array testing. This behavior suggests excessive turbulent diffusion and premature jet spreading. The RNG and Realizable $k-\epsilon$ models introduce modifications to the dissipation formulation and the behavior of the eddy viscosity designed to improve the responsiveness in regions of strong strain and shear. The RNG formulation incorporates additional terms derived from renormalization group theory [26] to better account for rapidly strained flows, while the Realizable model imposes constraints on the eddy viscosity coefficient to prevent artificial turbulence production in high-rotation

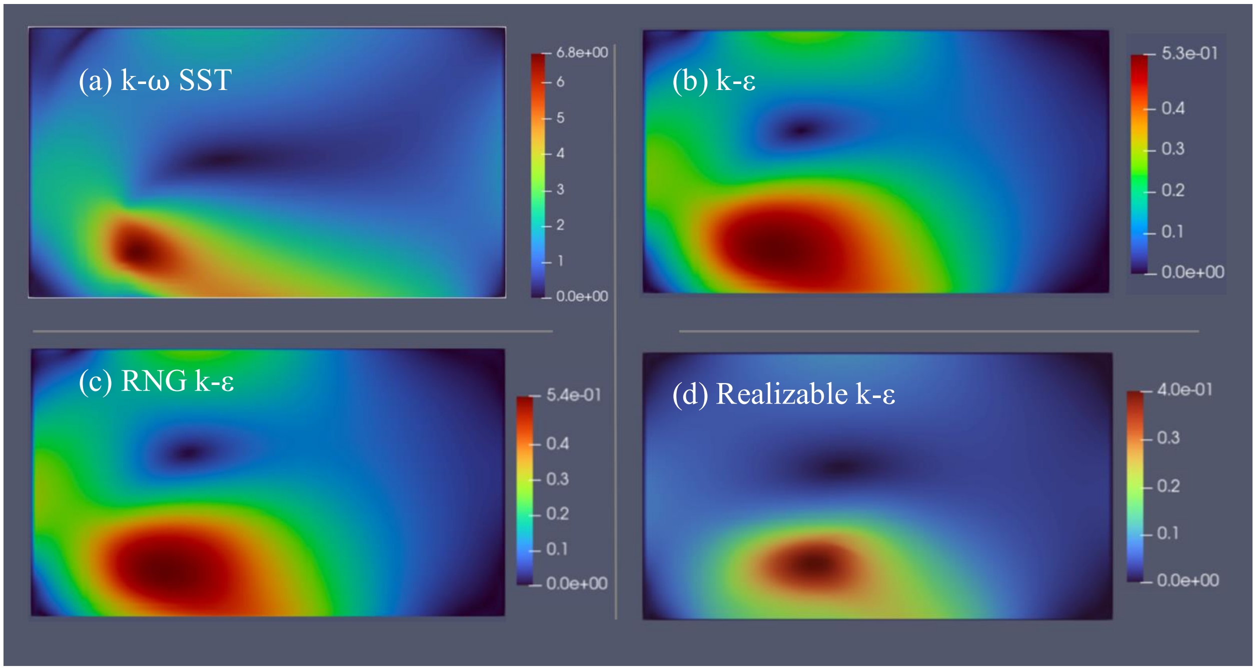

Fig. 2 Contours of the mean velocity magnitude U_{mag} at the centerplane of the fan array for (a) $k-\omega$ SST, (b) $k-\epsilon$, (c) RNG $k-\epsilon$, and (d) Realizable $k-\epsilon$ cases.

or high-strain regions. Similar RANS simulations [27] on jet arrays with 5 mm. diameter (lower Reynolds number and larger spacing between jets) employed $k-\epsilon$ (standard and RNG) and Reynolds Stress models. The standard $k-\epsilon$ was shown to capture the mean array behavior well compared to particle image velocimetry measurements. Showing that the mean flow behaviors of arrays can be captured. However, Ref. [27] used significantly higher resolution and a smaller domain without the effects of walls.

Figure 2 shows the average velocity magnitude on the fan array centerplane $(x-y)$ for all four cases. The $k-\omega$ case predicts a jet that quickly dissipates and is oriented towards the floor with a strong wall jet. The $k-\epsilon$ and RNG $k-\epsilon$ cases in Fig. 2(b) and (c), respectively, predict a wider jet that is oriented in the streamwise x direction. The jet velocity remains relatively constant for a longer distance compared to the $k-\omega$ case. While the jet spreads to the floor, there is far less dissipation, where the main jet core extends at least a full diameter of the fan array. Due to the extended jet and lower dissipation, the recirculation in the facility space is higher. The velocity behind the fan array and at the ceiling wall, which is entrained into the fans, is significantly higher compared to the $k-\omega$ case. Figure 2(d) shows the velocity magnitude of the realizable $k-\epsilon$. This case shows a rather different flow field where the velocity from the fan array peaks further downwind from the plane. Based on experimental measurements and known characteristics of jet arrays, the model does not seem to capture the flow correctly. This is most likely due to model coefficients that were not calibrated for this case. In fact, none of the default (i.e., published) coefficients for any models were changed. While calibration to some experimental data could help improve the model predictions, this is outside of the scope of this work.

The centerline streamwise velocity from each case is shown in Fig. 3. One of the main discrepancies identified in Ref. [14] was the differences between the centerline velocity of the RANS $k-\omega$ predictions and measurements from different array sizes. The experimental hot-wire anemometer measurements for a 3×3 and 9×9 configurations from the University of Memphis fan array are shown in Fig. 3 as well. A major difference between array sizes in the experiments is the formation of a core velocity region downwind in the array where individual jets merge. The core region does not appear in a 3×3 array where the velocity can be observed to decay steadily, similar to that of a canonical jet. On the other hand, the 9×9 array shows a nearly constant velocity region that persists downwind. The $k-\omega$ simulation clearly follows the steady decay, which would be expected for a canonical, single nozzle jet, and the trend of the 3×3 array, despite simulating a large 25×25 array, which is expected to have a large core region. The turbulence model is unable to predict the appearance of this region, which occurs due to the presence of multiple interacting jets upwind.

The $k-\epsilon$ models (standard and RNG) predict a longer jet and slower decay at the centerline as shown in Fig. 4. The jet decay matches the 9×9 array behavior closer, suggesting that the turbulence models are better at capturing

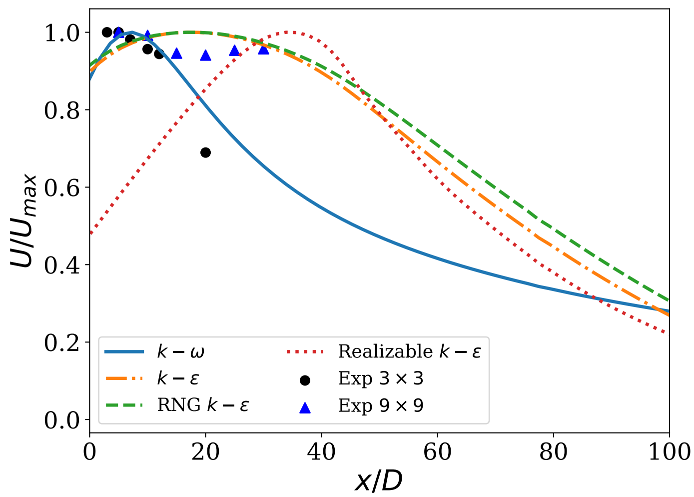

Fig. 3 Streamwise velocity through the centerline of the FAWT for each case (lines) and experimental measurements of 3×3 and 9×9 arrays (markers).

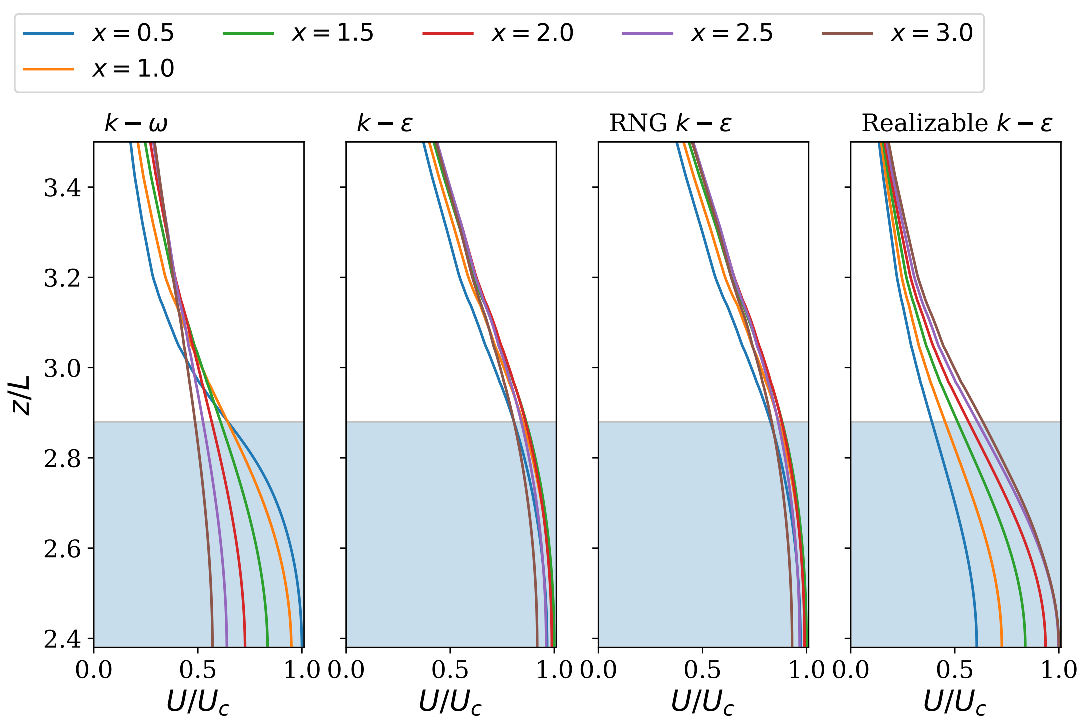

Fig. 4 Streamwise velocity profiles across the spanwise for each case at locations $x = 0.5, 1, 1.5, 2, 2.5$ and 3 m. downwind of the fan array.

free shear layer behavior expected for a fan array compared with the $k-\omega$ model. The realizable $k-\epsilon$ model shows acceleration from the fan array and quick decay, which is nonphysical.

Figure 4 shows the streamwise velocity profiles across the spanwise direction at locations $x = 0.5, 1, 1.5, 2, 2.5$ and 3 m. downwind for all turbulence cases. (See Fig. 1(a) for locations). The $k-\omega$ case shows the jet spreading with a large velocity gradient along the outer shear layer of the fan array decaying. On the other hand, the standard $k-\epsilon$ and RNG $k-\epsilon$ cases shows a relatively little decay within the first 3 m. of the fan array. Inside the fan array area, this is more consistent with the behavior observed in Ref. [14], where profiles obtained from experiments at a Caltech facility did not decay. However, there is a descrepancy in the outer shear layer behavior. The $k-\epsilon$ cases show that the velocity outside the array has been entrained into the jet, and a relatively small velocity gradient is predicted. Similar measurements from the Caltech dataset show that the outer shear layer and fan array jet are confined by a strong velocity gradient. This suggests that $k-\epsilon$ models overpredict entrainment compared to measurements, and further investigation is required.

V. Conclusion

This study investigated turbulence model sensitivity in predicting jet interaction and centerline velocity decay for a 25×25 fan array configuration. Previously, the $k-\omega$ SST model was used to perform RANS simulations; however, those simulations incorrectly predicted a sharp decay in centerline velocity that did not correlate well with physical experimental observations from large fan array tests. The jet centerline velocity decay resembled a canonical jet or a small array more closely. It was hypothesized that the RANS simulations failed to reproduce the sustained core velocity region observed for larger array configurations because they do not capture the appropriate turbulence behavior in the shear layers of the fan jets. The present comparison of standard $k-\epsilon$, RNG $k-\epsilon$, and Realizable $k-\epsilon$ formulations demonstrates that turbulence closure selection has a significant influence on predicted jet development and shear-layer behavior. The standard and RNG $k-\epsilon$ models produced a longer jet core and slower centerline decay, showing closer agreement with the experimental trends observed in the 9×9 configuration. In contrast, the $k-\omega$ SST model followed a canonical single-jet decay trend, which aligns well with the experimental behavior of the 3×3 configuration. However, when applied to the larger array, the $k-\omega$ SST model was unable to capture the sustained core velocity region produced by multiple interacting jets. The Realizable $k-\epsilon$ model produced nonphysical acceleration and rapid dissipation in the near field. These results suggest that $k-\epsilon$-based models more effectively capture free shear-layer interaction in large fan arrays compared to the previously used $k-\omega$ SST formulation. However, challenges remain in accurately predicting outer shear-layer gradients and entrainment behavior. Further investigation is needed to assess mesh sensitivity, turbulence model calibration, and potential higher-fidelity modeling approaches to improve predictive capability for large interacting jet systems. Continued development of improved turbulence closure strategies will be essential for guiding future fan array facility design and optimization.

References

[1] Albertani, R., Hubner, P., Ifju, P., Lind, R., and Jackowski, J., "Wind tunnel testing of micro air vehicles at low reynolds numbers," *SAE transactions*, 2004, pp. 1474–1486.

[2] Boschetti, P., Cárdenas, E., and Garcia, N., "Experimental Aerodynamic Study of UAV Wind Tunnel Model for Low Reynolds Number," *22nd Applied Aerodynamics Conference and Exhibit*, 2004, p. 4969.

[3] O'Donnell, R. S., and Mohseni, K., "Aerodynamic parameter estimation from wind tunnel testing of a small UAS," *2018 AIAA Atmospheric Flight Mechanics Conference*, 2018, p. 0294.

[4] Daida, J. M., Russell, P. B., Crawford, T. L., and Vesecky, J. F., "An unmanned aircraft vehicle system for boundary-layer flux measurements over forest canopies," *Proceedings of IGARSS'94-1994 IEEE International Geoscience and Remote Sensing Symposium*, Vol. 2, IEEE, 1994, pp. 1248–1250.

[5] Carbajo Fuertes, F., Wilhelm, L., and Porté-Agel, F., "Multirotor UAV-Based Platform for the Measurement of Atmospheric Turbulence: Validation and Signature Detection of Tip Vortices of Wind Turbine Blades," *Journal of Atmospheric and Oceanic Technology*, Vol. 36, No. 6, 2019, pp. 941–955. https://doi.org/10.1175/JTECH-D-17-0220.1.

[6] Sun, Y., Sude, B., Lin, X., Geng, B., Liu, B., Ji, S., Jing, J., Zhu, Z., Xu, Z., Liu, S., et al., "Quality evaluation for measurements of wind field and turbulent fluxes from a UAV-based eddy covariance system," *Atmospheric Measurement Techniques*, Vol. 16, No. 22, 2023, pp. 5659–5679.

[7] Kikitsu, H., Kanda, J., and Iwasaki, R., "Flow simulation by wind tunnel with computer-controlled multiple fans," *Journal of Wind Engineering and Industrial Aerodynamics*, Vol. 83, No. 1-3, 1999, pp. 421–429.

[8] Hangan, H., "The wind engineering energy and environment (WindEEE) dome at Western University, Canada," *Wind Engineers, JAWE*, Vol. 39, No. 4, 2014, pp. 350–351.

[9] Noca, F., Catry, G., Bosson, N., Bardazzi, L., Marquez, S., and Gros, A., "Wind and Weather Facility for Testing Free-Flying Drones," *AIAA Aviation 2019 Forum*, American Institute of Aeronautics and Astronautics, 2019. https://doi.org/10.2514/6.2019-2861, URL https://arc.aiaa.org/doi/10.2514/6.2019-2861.

[10] Walpen, A., Catry, G., and Noca, F., "Real-scale atmospheric wind and turbulence replication using a fan-array for environmental testing and UAV/AAM validation," *AIAA SCITECH 2023 Forum*, 2023, p. 0812.

[11] Zhao, L., Zhang, L., Cui, W., Cao, S., and Ge, Y., "The reproduction of 2-D non-synoptic wind field in an actively controlled wind tunnel," *Journal of Wind Engineering and Industrial Aerodynamics*, Vol. 251, 2024, p. 105786.

[12] Li, S., Liu, Y., Jiang, Z., Hu, G., Noack, B. R., and Raps, F., "Aerodynamic characterization of a fan-array wind generator," *AIAA Journal*, Vol. 62, No. 1, 2024, pp. 291–301.

[13] Di Luca, M., Leipold, M., and Noca, F., "On the generation of plane compound shear flows with fan-array wind tunnels," *AIAA SCITECH 2024 Forum*, 2024, p. 2672.

[14] Rahmati, M., Rahman, M. R. U., Nouri, R., Dougherty, C., Robinson, D., Narsipur, S., White, C., Foti, D., and Jacobs, E., "Assessment and Comparison of Fan Array Wind Tunnel Facilities," *AIAA SCITECH 2026 Forum*, 2026, p. 2307.

[15] Menter, F. R., Kuntz, M., and Langtry, R., "Ten Years of Industrial Experience with the SST Turbulence Model," *Turbulence, Heat and Mass Transfer 4*, edited by K. Hanjalic, Y. Nagano, and M. Tummers, International Symposium on Turbulence, Heat and Mass Transfer, Begell House, Inc., Antalya, Turkey, 2003, pp. 625–632. Proceedings of the 4th International Symposium on Turbulence, Heat and Mass Transfer.

[16] Weller, H. G., Tabor, G., Jasak, H., and Fureby, C., "A tensorial approach to computational continuum mechanics using object-oriented techniques," *Computers in Physics*, Vol. 12, No. 6, 1998, pp. 620–631. https://doi.org/10.1063/1.168744.

[17] Greenshields, C. J., and Weller, H. G., *Notes on computational fluid dynamics: general principles*, CFD Direct Limited, Reading, UK, 2022.

[18] Issa, R., "Solution of the implicitly discretised fluid flow equations by operator-splitting," *Journal of Computational Physics*, Vol. 62, No. 1, 1986, pp. 40–65. https://doi.org/10.1016/0021-9991(86)90099-9.

[19] Ferziger, J. H., Perić, M., and Street, R. L., *Computational Methods for Fluid Dynamics*, Springer International Publishing, Cham, 2020. https://doi.org/10.1007/978-3-319-99693-6.

[20] Patankar, S., and Spalding, D., "A calculation procedure for heat, mass and momentum transfer in three-dimensional parabolic flows," *International Journal of Heat and Mass Transfer*, Vol. 15, No. 10, 1972, pp. 1787–1806. https://doi.org/10.1016/0017-9310(72)90054-3.

[21] Patankar, S. V., *Numerical Heat Transfer and Fluid Flow*, 1st ed., CRC Press, 2018. https://doi.org/10.1201/9781482234213.

[22] Menter, F. R., and Esch, T., "Elements of Industrial Heat Transfer Prediction," *Proceedings of the 16th Brazilian Congress of Mechanical Engineering (COBEM 2001), Invited Lectures*, Vol. 20, Brazilian Society of Mechanical Sciences and Engineering, Uberlândia, Brazil, 2001, pp. 119–127.

[23] Launder, B. E., and Spalding, D. B., "The numerical computation of turbulent flows," *Numerical prediction of flow, heat transfer, turbulence and combustion*, Elsevier, 1983, pp. 96–116.

[24] Shih, T.-H., Liou, W. W., Shabbir, A., Yang, Z., and Zhu, J., "A new k- eddy viscosity model for high reynolds number turbulent flows," *Computers & fluids*, Vol. 24, No. 3, 1995, pp. 227–238.

[25] Yakhot, V., Orszag, S. A., Thangam, S., Gatski, T., and Speziale, C., "Development of turbulence models for shear flows by a double expansion technique," *Physics of Fluids A: Fluid Dynamics*, Vol. 4, No. 7, 1992, pp. 1510–1520.

[26] Wilson, K. G., "The renormalization group and critical phenomena," *Reviews of Modern Physics*, Vol. 55, No. 3, 1983, p. 583.

[27] Svensson, K., Rohdin, P., Moshfegh, B., and Tummers, M. J., "Numerical and experimental investigation of the near zone flow field in an array of confluent round jets," *International Journal of Heat and Fluid Flow*, Vol. 46, 2014, pp. 127–146.